# Photometric modelling for laboratory measurements of dark volcanic sand

Olli Wilkman[a,*], Maria Gritsevich[b,c,d], Nataliya Zubko[b], Jouni I. Peltoniemi[a,b], Karri Muinonen[a,b]

[a]*Department of Physics, P.O. Box 64, FI-00014 University of Helsinki, Finland*
[b]*Finnish Geospatial Research Institute, P.O. Box 15, FI-02431 Masala, Finland*
[c]*Department of Computational Physics, Dorodnicyn Computing Centre of the Russian Academy of Sciences, Vavilova St. 40, 119333 Moscow, Russia*
[d]*Institute of Physics and Technology, Ural Federal University, Mira St. 19, 620002 Ekaterinburg, Russia*

**Abstract**

We have performed laboratory measurements of the bidirectional reflectance factor (BRF) of a sample of dark volcanic sand. The measurements were carried out with three different treatments of the sample to produce different porosity and roughness characteristics. We model the measured BRF with a semi-numerical scattering model for particulate media, meant especially for dark planetary regoliths. We compare the BRF in two different spectral bands, 500–600 nm and 800–900 nm. The particulate medium (PM) scattering model is found to fit the measured data well, with a phase function representing the differences between the spectral bands. The interpretation of the physical parameters of the PM model is qualitatively sound, but remains somewhat uncertain due in part to the difficulty of characterizing the measured sample.

*Keywords:* photometry, regolith, shadowing

## 1. Introduction

For most of the bodies in the Solar System, the only sources of data available to us are photometry, spectrometry, and polarimetry. For the great majority, these properties can be observed only as disk-integrated quantities as the bodies are too small to resolve with our telescopes. In a few cases, images taken by spacecraft show a disk-resolved view of the surface and only a handful of objects have been actually studied up close by a variety of scientific instruments.

A good understanding of the spectral reflection properties of these objects is necessary in order to make most of the observed data. Disk-integrated spectrometry allows, e.g., for asteroid classification by spectral type, which indicates the mineral composition [4], and photometric lightcurves allow the determination of an asteroid's rotation state and shape [12]. A good reflectance model is also necessary for the photometric correction of imaging data of planetary surfaces taken by spacecraft [6]. Images taken in different illumination geometries can be compared and analysed together only after the effects of the geometry have been taken into account.

Due to the Apollo missions, the lunar regolith is the best understood of the planetary surface materials and serves as a prototype for the regoliths of other atmosphereless bodies such as the asteroids. It is formed from basaltic and anorthositic lunar rocks broken up by micrometeorites, thermal stress and solar radiation [15]. Volcanic basalt on Earth is used to produce regolith analogs, which approximate the chemical and physical properties of the samples returned from the Moon [16].

Many models for the reflectance of regolith-covered Solar System bodies have been developed, such as those of Lumme and Bowell [14], Hapke [10] and Shkuratov [24]. Li et al. [13] provide an up-to-date review on models applied to asteroid photometry.

*Corresponding author. Tel.: +358 9 19151007
*Email address:* olli.wilkman@helsinki.fi (Olli Wilkman)

Many laboratory studies of various regolith analogues exist in the literature, usually focused on one particular detail, such as the opposition effect features [25, 3], the effects of packing density [18, 9], estimating the parameters of a particular model or family of models [5, 23], or comparing different models. Johnson et al. [11] study several different lunar and martian regolith analogues as well as real lunar regolith samples.

The purpose of this study is to test a model presented by Wilkman et al. [27], which describes the reflectance of a particulate surface through a combination of the scattering properties of individual grains and a correction for the particulate packing. We apply the model to a sample of dark volcanic sand to demonstrate its applicability in modelling surfaces such as the lunar regolith.

In Section 2, we review the theory of bidirectional reflectance. In Section 3, we describe the experimental setup and the sample we have measured. In Section 4, the numerical reflectance model we use is described. Section 5 presents the results of the measurements and modelling and Section 6 describes our conclusions.

## 2. Theory

The reflectance behaviour of a surface is described by its bidirectional reflectance factor (BRF). In general, the BRF is a function of four angles: $\theta_i$ and $\phi_0$ are the zenith and azimuth angles of incidence, $\theta_e$ and $\phi$ are the zenith and azimuth angles of emergence. Additionally, the phase angle $\alpha$, the complement of the scattering angle is used. The BRF is also a function of the wavelength of light. The cosines of the zenith angles $\mu_0 = \cos\theta_i$ and $\mu = \cos\theta_e$ are widely used for convenience.

If the target is horizontally and azimuthally isotropic, the functional dependence is reduced to three variables, as the only azimuthal variable is the difference $\phi - \phi_0$. In the present study, this is assumed to be the case, and we set $\phi_0 = 0°$. The geometric definitions of the angles are given on Figure 1. When $\phi = 0$, the incident and emergent directions are on the same side of the zenith.

The BRF is defined as a ratio of the reflected light intensity of a given target to an ideal Lambertian reflector with a spherical albedo of unity under same incident irradiation:

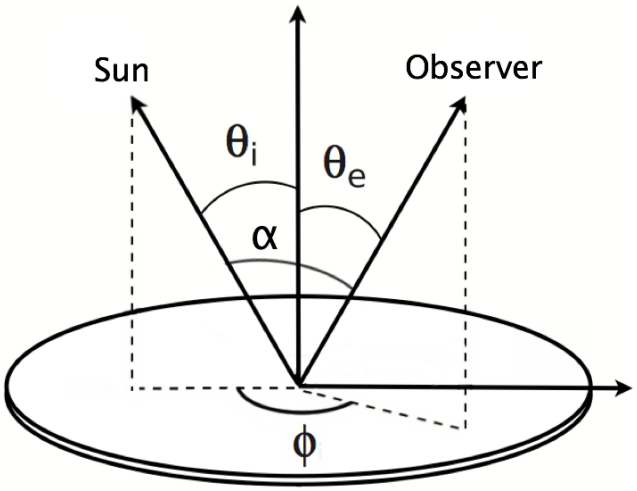


Figure 1: The illumination geometry.

$$\mathrm{BRF}(\mu, \mu_0, \phi, \phi_0) = \frac{I(\mu, \phi)}{\mu_0 I_0(\mu_0, \phi_0)} \qquad (1)$$

where $I_0$ is the incident collimated flux, $I_0(\Omega) = \pi F_0 \delta(\Omega - \Omega_0)$, and $I(\mu, \phi)$ is reflected radiance. This definition makes the BRF equal to the reflection coefficient $R$ of the surface, which relates the incident flux $\pi F_0$ to the reflected intesity,

$$I(\mu, \mu_0, \phi, \phi_0) = \mu_0 R(\mu, \mu_0, \phi, \phi_0) F_0, \qquad (2)$$

because the reflection coefficient for a Lambertian surface is unity, $R_\mathrm{L} = 1$.

BRFs of typical remote sensing targets vary greatly. Some targets are forward scattering, some are backward scattering, some have a strong specular reflection, some reflect highly to low zenith angles [19, 22, 20, 21, 29]. Each target has its unique BRF that depends on all of its geometrical and physical properties. Thus the BRF information can be a valuable tool in target classification and quantification.

The *plane albedo* $A_p(\mu_0)$ is the fraction of the incident flux scattered by a planar surface into the whole sky hemisphere. The plane albedo is a property of the surface and a function of the incident light direction,

$$A_P(\mu_0, \lambda) = \frac{1}{\pi} \int\int \mu R(\mu_0, \mu, \phi, \lambda)\, \mathrm{d}\mu\, \mathrm{d}\phi, \quad (3)$$

where $\lambda$ is the wavelength of the light. In principle, the integrations in Eq. 3 run over full hemispheres and wavelength range, but in many practical applications the observational range may be limited to a smaller wavelength range, e.g., only visual light, and the field of view of the instrument is also often limited; typical albedometers see zenith angle ranges of $\pm 70^\circ$ to $\pm 80^\circ$.

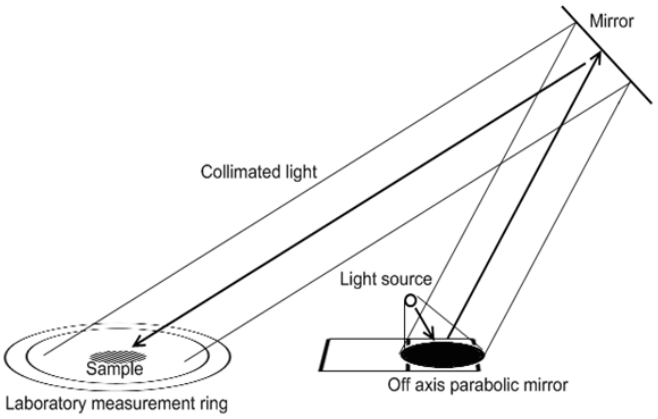


Figure 2: The laboratory illumination set-up.

## 3. Laboratory measurements

### *3.1. The measurement apparatus*

The BRF measurements have been taken using the Finnish Geodetic Institute Field Goniospectrometer FIGIFIGO, an automated portable instrument for multi-angular reflectance measurements. The FIGIFIGO system consists of a motor-driven moving arm that tilts up to $\pm 90^\circ$ from the vertical, optics at the end of the arm, and an ASD FieldSpec Pro FR 350–2500 nm spectroradiometer. The active optics system at the top of the measurement arm has been built using lenses and Thorlabs lens tube system components. The signal from the sample comes to the optics through a servo-driven mirror. The turnable mirror allows the control computer to stabilize spectrometer field-of-view at the sample within accuracy of 1 cm from all zenith directions even if the sample is not positioned exactly at the center of rotation. The length of the telescopic measurement arm is adjustable from 1.55 to 2.65 m and it houses an inclinometer to provide the control computer with the measured zenith angle. A detailed description of the instrument can be found in [8] and [22].

Typically, the detector footprint diameter is about 10 cm, elongating at larger sensor zenith angles as $1/\cos\theta$, and wandering around a few centimeters due to material flexing and with azimuthal movements.

The illumination scheme in the laboratory is presented in Figure 2. In the laboratory experiments, a halogen lamp is used as a light source. The lamp light is collimated by a parabolic mirror and directed to the target by a plane mirror. The illuminated area of the sample is large enough to contain the footprint in all of the viewing geometries used.

The instrument has been calibrated by taking a nadir measurement from a Labsphere Spectralon 25× 25 cm white reference plate before and after each measurement sequence. The Spectralon target is not perfectly Lambertian, but its BRF has been measured separately and the deviance from Lambertian scattering is taken into account in the calibration [22]. The Spectralon has been levelled horizontal with a bubble level with an accuracy of about $1^\circ$.

For the laboratory experiments, the system is mounted on a rotating ring, which allows making the measurements at controlled azimuth angles. The measurements are always started at $0^\circ$ relative azimuth (principal plane). The measurement arm slowly moves between the selected zenith angle range (in our experiment it was set to $\pm 70^\circ$ from the zenith) while the spectrometer is continuously recording data. Measurement of one hemisphere at one illumination angle takes between 15 and 30 minutes, depending on the expected results and accuracy, and various technical aspects.

The accuracy of the spectral BRF measurements using FIGIFIGO is estimated to be 2% in the visible band. The angle registration accuracy is $2^\circ$.

The measured unnormalised radiance spectra $I(\lambda)$ is normalised by measured nadir spectra from a reference target, $I_{\mathrm{std}}(\lambda)$, as

$$\mathrm{BRF}(\mu, \mu_0, \phi, \phi_0; \lambda) = \frac{I(\lambda)}{I_{\mathrm{std}}(\lambda)} R_{\mathrm{std}}, \quad (4)$$

where $R_{\mathrm{std}}$ is the reflectance of the Spectralon reference target.

### 3.2. The volcanic sand measurement

Our sample material is volcanic sand, mostly made of basaltic to andesitic poorly crystallized glass particles, dark grey to black in color. The sample was earlier described and studied in particular in the frame of the Soot on Snow experiment [17, 20, 26]. The sample is a mixture of the volcanic ash of glaciofluvial nature, originating from under the Mýrdalsjökull glacier, which may be mixed with the ash of the Eyjafjallajökull eruption in 2010 and the Grímsvötn eruption in 2011. It represents well the material resuspended in the most active dust source in Southern Iceland and deposited on glaciers or snow in the south and southeast Iceland [1, 2]. The collecting site was in the Mýrdalssandur dust source in the south Iceland in November 2012, and this material has been mixed by aeolian processes, with enriched sand proportion as the silt sized material is lost as dust along the way. The sample was sieved and consisted mostly of particles between 250–1300 $\mu$m. This size range is larger than the typical Lunar surface regolith, which has a mean particle size around 100 $\mu$m. Figure 3 shows the sample in its plastic container before the measurements.

The sample was treated in three different ways. For the first measurement, the material was sieved onto a dark cloth on a plate forming a layer approximately 1 cm thick (Figure 4, top). For the second measurement, the plate was vibrated by knocking on its bottom, causing the material both to settle and form a rippled surface structure (Figure 4, middle). For the third measurement, the ripples were smoothed by dragging a plastic ruler lightly across the surface and then the material compacted all around by pressing with the flat side of the ruler (Figure 4, bottom).

A fixed incident angle of 52° was used for all three samples. Additionally, the same material, prepared in the same way as the "sieved" sample, was measured at two other incident angles: 38° and 60°. These additional data are treated as a separate fourth sample.

The data cover a phase angle range from approximately 5° to 122°. The emergence angle $\theta_e$ was swept from −70° to +70° at seven different azimuth angles, $\phi = 0°, 5°, 10°, 20°, 45°, 60°$, and 90°. To improve signal-to-noise ratio, the measurement at each azimuth angle was repeated 5 times.

Figure 3: The sample in normal room illumination before being sieved onto the measurement plate.

Figure 5 shows the spectrum of the sieved sample under normal viewing. We separate two spectral bands from the data: 500–600 nm, which we call "green" and 800–900 nm, which we call "NIR". We have therefore eight different data sets, corresponding to the four sample treatments and two wavelength bands.

## 4. The scattering model

We use a semi-numerical scattering model for rough particulate surfaces [27], which has previously been applied to disk-resolved photometric data of the lunar surface [28]. The model has the reflection coefficient

$$R_{PM} = \frac{\omega_V}{4} P_V(\alpha) S(\mu_0, \mu, \phi) \frac{1}{\mu_0 + \mu}, \qquad (5)$$

where $\omega_V$ is the *volume-element albedo*, $P_V$ is the *volume-element phase function*, and $S(\mu_0, \mu, \phi)$ is the

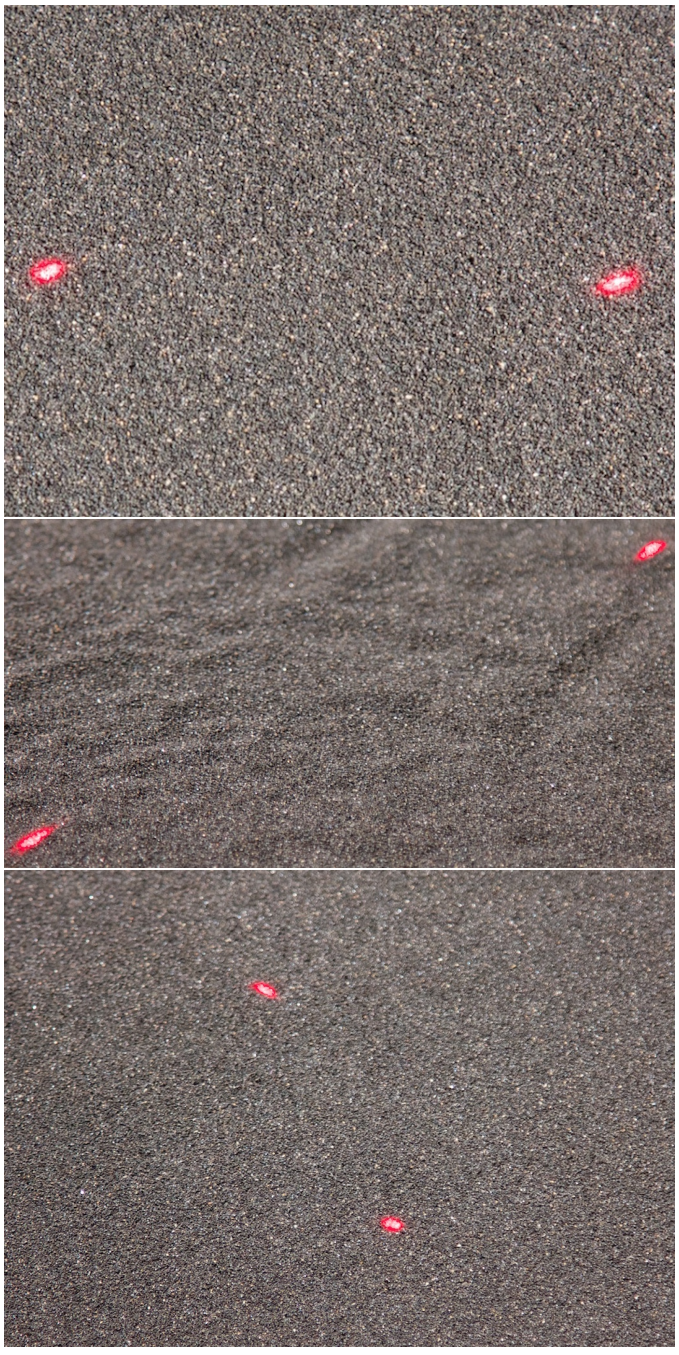

Figure 4: Close-up photographs of the samples on the measurement plate under 52° illumination by the laboratory light source. The sieved sample is on the top, shaken in the middle, and smoothed on the bottom. The two laser dots are alignment guides for the FIGIFIGO optics, and are approximately 10 cm apart on the surface. The lasers are switched off during the measurement.

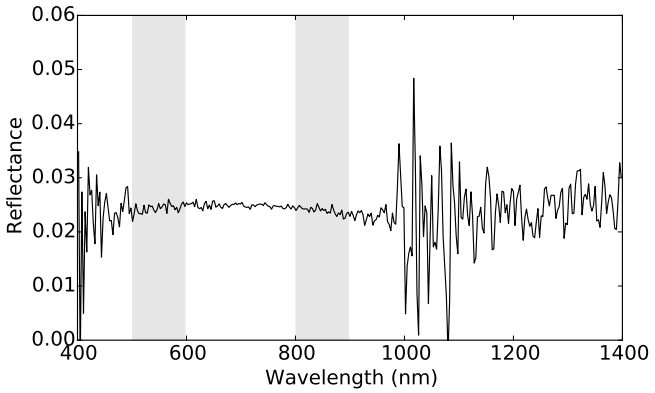


Figure 5: The spectrum of the sieved sample under normal viewing and 52° incidence. The shaded areas show the two spectral bands used in this study. For illustration purposes, the data have been smoothed by a 3 nm average binning.

*shadowing correction*. The albedo and the phase function describe the scattering properties of individual particles of the regolith. The shadowing correction takes into account the effects of the porous particulate structure and depends on various properties of the surface, mainly the packing density and surface roughness. We use pre-computed values of $S$, available in a public database[1] covering various surface parameters.

The shadowing correction $S$ is derived from ray-tracing simulations in a medium of packed particles with a uniform distribution of diameter. The packing density $\nu$ can range from 15% to 55%. In addition, macroscale roughness can be added by intersecting the medium with a random height map and removing all particles above it. This height map has fractal statistics, controlled by the Hurst exponent $H$, which determines the horizontal correlation of the heights, and scaled by the amplitude parameter $\sigma$.

The packing density $\nu$ has the largest effect on the shape of the BRF, which is then further modified by surface roughness. The effect of increasing roughness amplitude $\sigma$ is to reduce the forward scattering and to make the surface darker at high zenith angles. In addition, at a given value of $\sigma$, higher values of $H$ lead to a wider opposition effect and stronger forward scattering. Figure 6 illustrates the effects of different parameter values on the BRF.

[1] https://wiki.helsinki.fi/display/PSR/Numerical+Scattering+Law

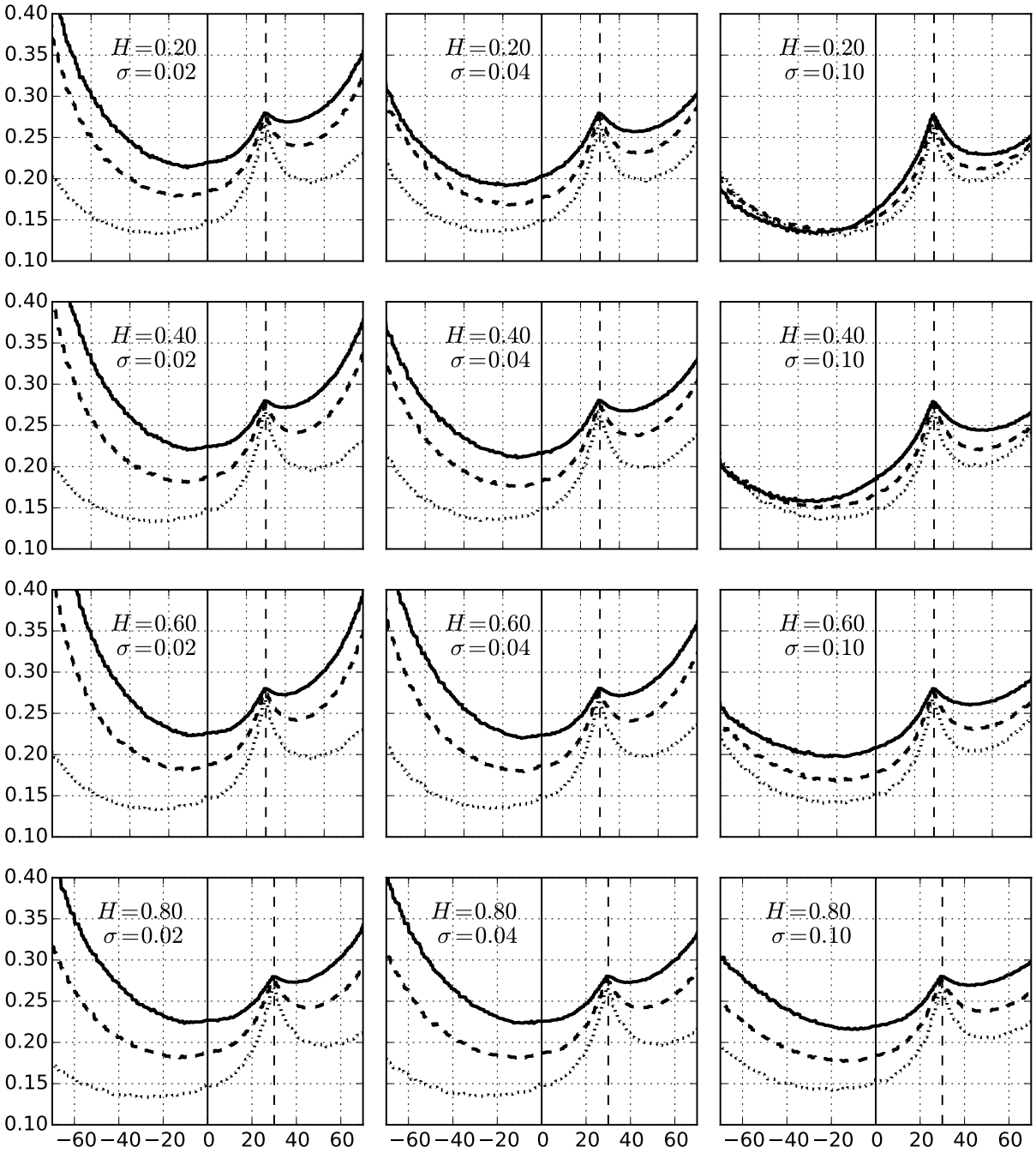


Figure 6: The values of the PM scattering model with an isotropic phase function, at $\phi = 0°$ and $30°$ incidence. Three different packing densities are shown: $\nu = 0.55$ (solid line), $\nu = 0.30$ (dashed line) and $\nu = 0.15$ (dotted line).

We vary $H$ from 0.20, corresponding to a "spiky" surface of narrow features, to 0.80, which corresponds to wide and smooth features. The amplitude $\sigma$ ranges from zero to 0.10. Approximately equating the simulation units to the estimated size range of the measured sample, the maximum amplitude $\sigma = 0.10$ corresponds to a standard deviation of height of 4.3 millimeters. With nine different packing densities, four values of the Hurst exponent and seven different amplitudes there are a total of 216 different choices of the shadowing correction $S$.

Because the data do not cover the entire range of phase angles, and $P_V(\alpha)$ is normalized over phase angle, it is not possible to separate the product $\omega_V P_V(\alpha)$. We model this product with a cubic spline function with nodes at $\alpha = 0°, 10°, 40°, 90°, 130°$ and $180°$. The derivatives at the endpoints were set to zero, so there are six real-valued parameters in the model, in addition to the choice of the shadowing correction out of the 216 different discrete values. We choose the spline approach for its greater flexibility compared to phase functions such as a linear combination of Henyey-Greenstein functions. In order to model the opposition effect as well as the broader forward and backward scattering peaks, at least three Henyey-Greenstein components would be needed. Experimentation showed that the spline produces a good fit with the same number of free parameters and a simpler optimization procedure.

An assumption of the PM model is that $\omega_V P_V(\alpha)$ depends mainly on the properties of the individual surface particles and the wavelength of light, while the shadowing correction $S$ depends only on the way the particles are arranged. It is therefore possible to separate these two effects. We fit the shadowing correction and the phase function to our eight data sets simultaneously (two spectral bands and four sample treatments), so that the phase function is the same for every data set in the same spectral band, while the shadowing correction is the same for the different sample treatments.

The fit is done with a stochastic optimization algorithm, which performs a random walk in the parameter space for the spline coefficients, preferring to move toward better fitting models. For each proposed phase function, the fit to the data is computed with each of the 216 different shadowing corrections and the best combination is kept. The procedure produces robust results, converging to the same best-fit parameters from different starting points.

We also compared the results to the Lommel-Seeliger model [7] which is widely used in studies of Solar System photometry. The Lommel-Seeliger model derives from radiative transfer theory in a homogeneous and sparse medium of scatterers. It does not take into account the particulate nature of the material, which affects the extinction statistics of the light depending on the illumination geometry.

## 5. Results

The measured data and best-fit model curves are shown in Figures 7 and 8, at zero azimuth angle, which represents one seventh of the total amount of data. There are significant differences both between the different sample treatments, and between the two spectral bands. For a given sample treatment, the NIR band always has stronger forward scattering and weaker backward scattering than the green band. In both spectral bands, the shaken sample is overall brighter than the sieved one by about 25%, but the balance between forward and backward scattering remains the same. After the shaken sample is smoothed, it becomes less backward scattering and more forward scattering.

The PM model is able to fit the measured BRF well. In the principal plane, there is a slight discrepancy around $-50°$ zenith angle for most of the samples. In other azimuthal planes this is not apparent. There is some stepping and numerical noise apparent in the best-fit curves, due to the finite resolution of the shadowing correction part of the PM model.

Figure 9 shows the best-fit function for $\omega_V P_V(\alpha)$ for each spectral band. These curves represent the average scattering properties of the volume elements, i.e., individual grains and their immediate surroundings, in the sample. The difference in the forward and backward scattering intensities is apparent here.

Table 1 shows the best-fit parameters of the shadowing correction for each sample. The shaken sample shows a clear deviation in the best-fit packing density compared to the other two. We discuss a possible cause for this below.

| | $\nu$ | $H$ | $\sigma$ | $p$ green | $p$ NIR |
|---|---|---|---|---|---|
| sieved | 0.35 | 0.40 | 0.10 | 0.043 | 0.038 |
| shaken | 0.55 | 0.40 | 0.08 | 0.044 | 0.039 |
| smooth | 0.45 | 0.20 | 0.06 | 0.043 | 0.039 |
| sieved 2 | 0.30 | 0.60 | 0.10 | 0.043 | 0.038 |

Table 1: The best-fit parameters for the shadowing correction, as well as the geometric albedo under normal incidence computed from the best-fit models.

Another unexpected feature is that the BRF of the second sieved sample is closer to the smooth sample more than to the first sieved sample. This is not apparent from the packing density alone, but the much lower Hurst exponent produces a very different roughness effect, which leads to a result similar to the smooth surface.

We can then use the best-fit reflection coefficient to extrapolate the BRF in any illumination. Figure 10 shows the BRF under normal illumination for all of the models. Under normal illumination, the differences between different models are the greatest. Here the similarity between the second sieved sample and the smoothed first sample is clear. The differences between the spectral bands are also apparent.

We can also use the best-fit reflection coefficient to compute the geometric albedo of a flat disk in normal illumination. The geometric albedo is defined as the disk-integrated brightness at zero phase angle divided by that of a Lambertian disk. It is found to be approximately 0.039 in the NIR band and 0.043 in the green band for all of the samples. The geometric albedos of spheres with the same reflection coefficients are 2–3% lower in every case.

The uncertainty in the geometric albedos from our parameter estimation scheme is on the order of ±0.001. However, because of the lack of data at low phase angles, as well as the angular size of the light source ($\approx 2^\circ$) and the acceptance angle of the optics ($\approx 3.7^\circ$), these values are uncertain. The opposition effect is underestimated, and the real geometric albedo is likely to be higher. Still, the values show that the NIR band is brighter near opposition than the green band.

Because the data also do not contain phase angles greater than 130°, the volume-element phase function is unconstrained in the forward scattering direction. These ranges of missing data at low and high phase angles prevent reliable estimation of photometric quantities which are integrated over the phase angle. It also prevents us from separating the product $\omega_V P_V(\alpha) \equiv f(\alpha)$, because the normalization of $P_V(\alpha)$ is an integral over the phase angle. From this normalization follows that

$$\omega_V = \frac{1}{2}\int_0^\pi f(\alpha)\sin\alpha\,\mathrm{d}\alpha \qquad (6)$$

The true values of the phase function in the unconstrained regions are almost certain to be higher than the fitted curve, and therefore the above equation provides a lower bound for the true value of $\omega_V$. The unconstrained regions also have a lower weight in the integral due to the $\sin\alpha$ term. We find that the best-fit spline in Figure 9 gives $\omega_V \geq 0.19$ in green and $\omega_V \geq 0.21$ in NIR.

The plane albedo (Equation 3) of the material can also be computed from the model fits (Figure 11). Its values also become less certain when the integration requires phase angles greater than 130°, i.e. when the incidence angle is greater than 40°. In the NIR band, the plane albedo at normal incidence is about 4% lower than in the green band, but grows faster with increasing incidence angle and by 50° incidence they are equal. The uncertainty in the individual curves is around 1%. This relationship does not depend on the shadowing correction. Here, too, we see the similarity between the smooth sample and the second sieved sample.

## 6. Discussion

We have measured a sample of dark volcanic sand and obtained a good data set with low noise in the visible and near-infrared. We also obtained a lower-quality set of data at different incidence angles. We fit the particulate medium scattering model to the measured data, fitting the volume-element properties separately in two spectral bands. The model provides a consistent and good-quality fit.

The increase in modelled packing density for the shaken sample is surprising. We do expect the packing density to increase slightly from the shaking, but

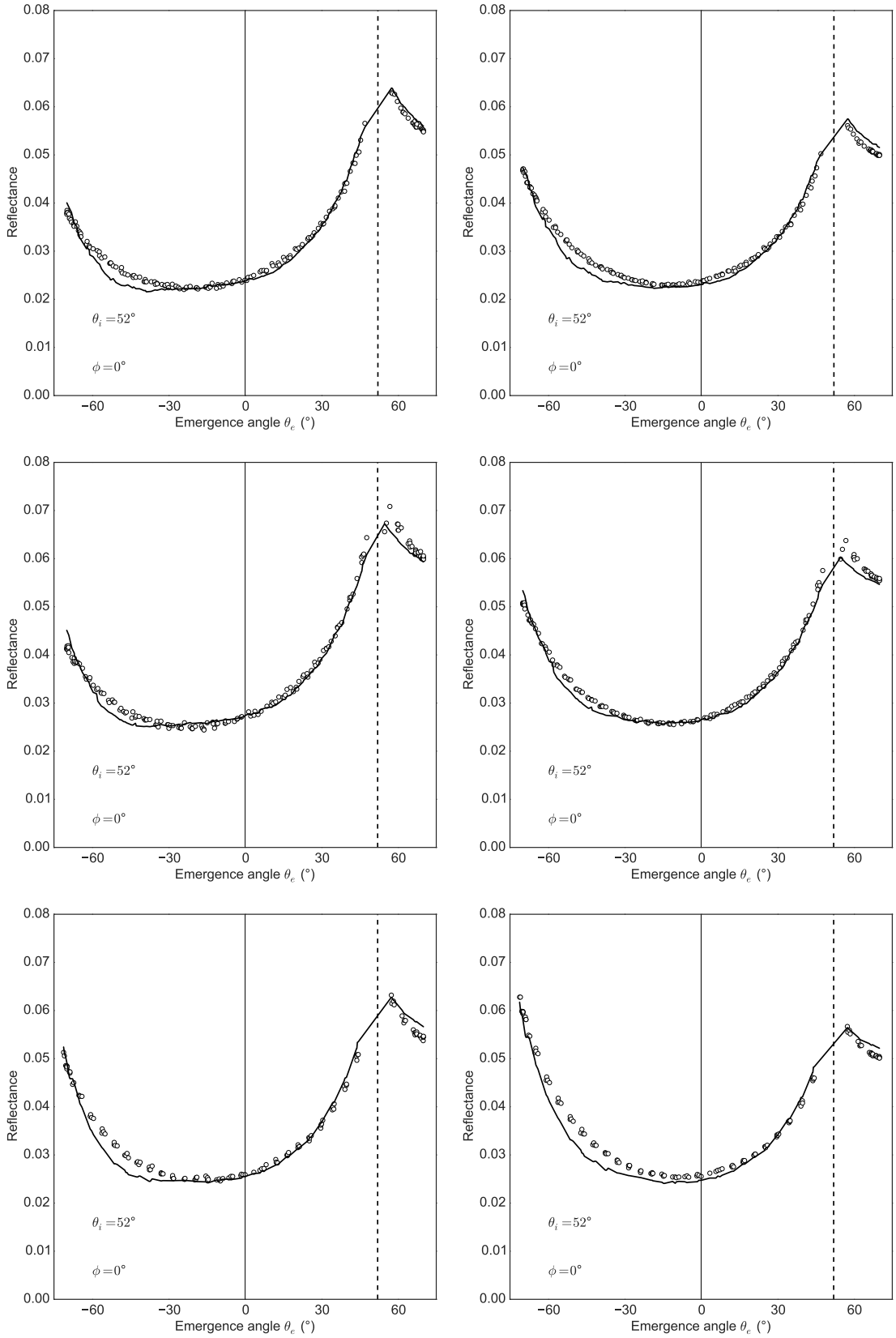


Figure 7: The measured normalized brightness (circles) and best fit (black line) in the principal plane ($\phi$ = 0) for the sieved (top row), shaken (middle row) and smooth (bottom row) samples. The left column shows the green spectral band and the right column the NIR band. The horizontal axis is the angle of emergence $\theta_e$, with the zenith direction in the middle. The vertical dashed line indicates the incident direction.

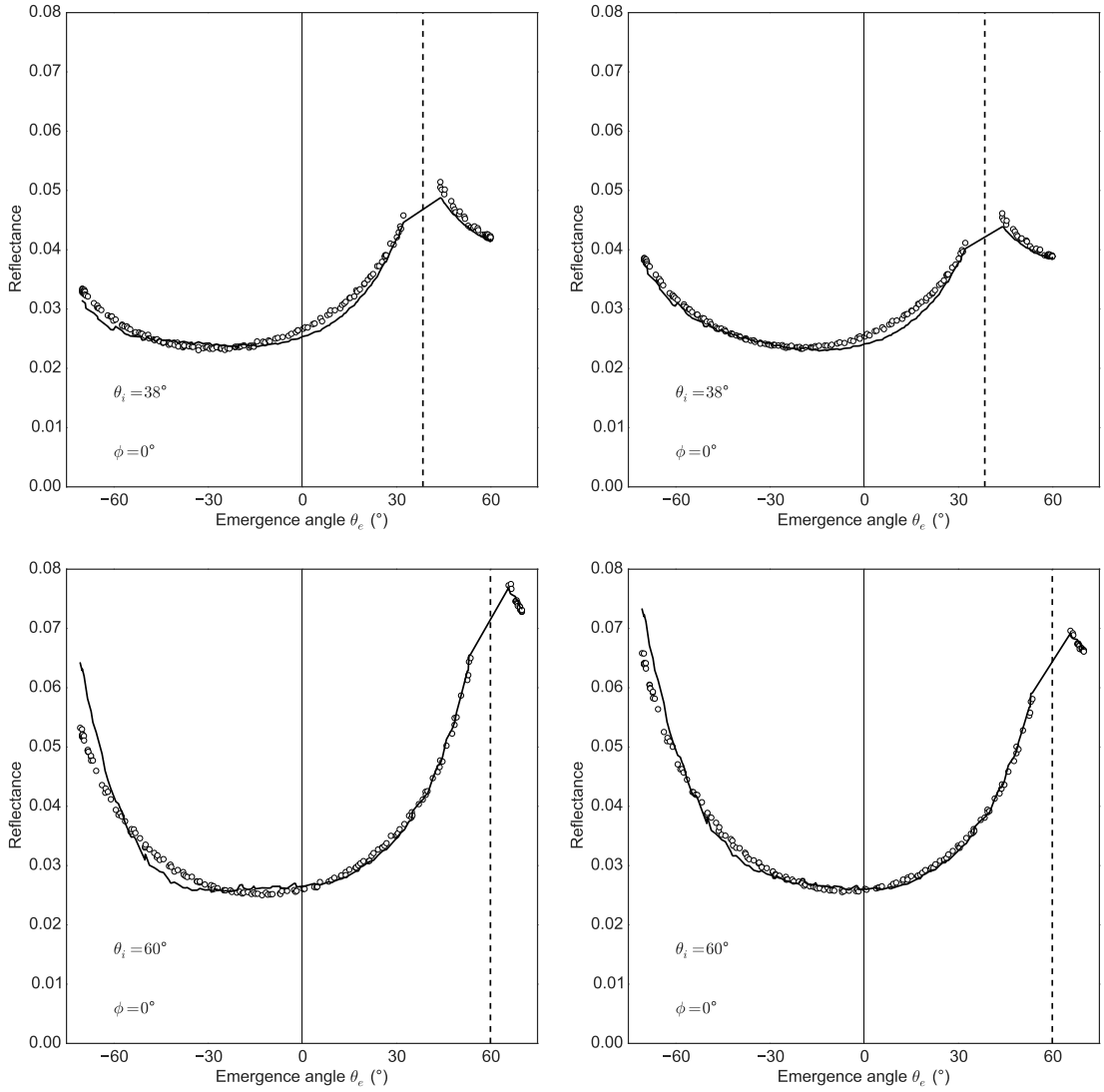


Figure 8: As Fig. 7 but for the two additional incidence angles with a sieved sample.

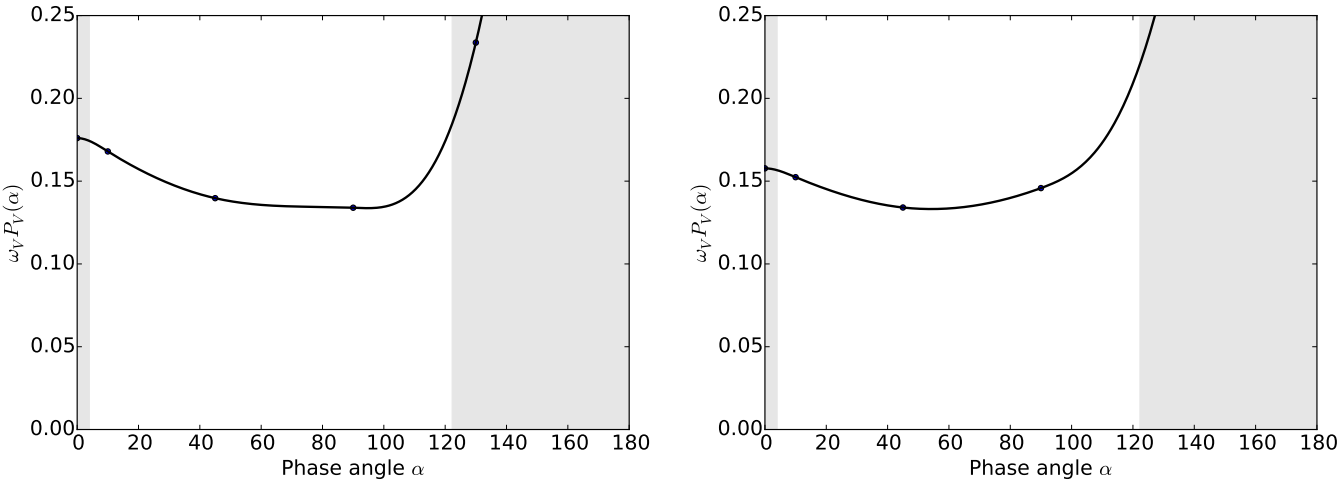


Figure 9: The best-fit spline for the volume-element albedo and phase function product $\omega_V P_V(\alpha)$ for the green (left) and NIR (right) measurements. The grey shading indicates phase-angle ranges where data were not available.

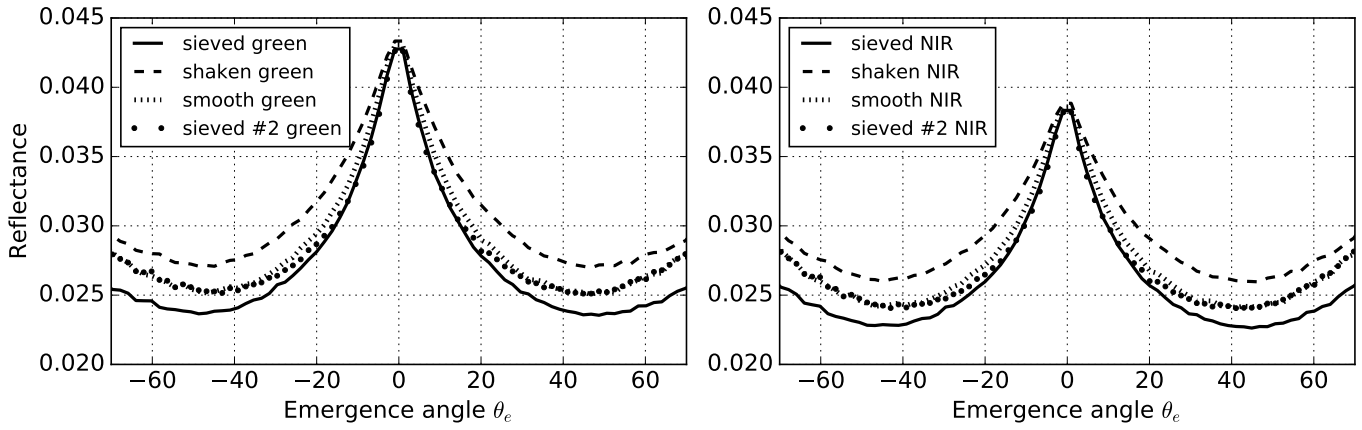


Figure 10: The BRF of all the samples, reduced to normal illumination with the best-fit models. In normal illumination the horizontal axis corresponds both to the angle of emergence and the phase angle and the BRF is azimuthally symmetric. The four different surface treatments correspond to different shadowing corrections, and the two different spectral bands to different phase functions.

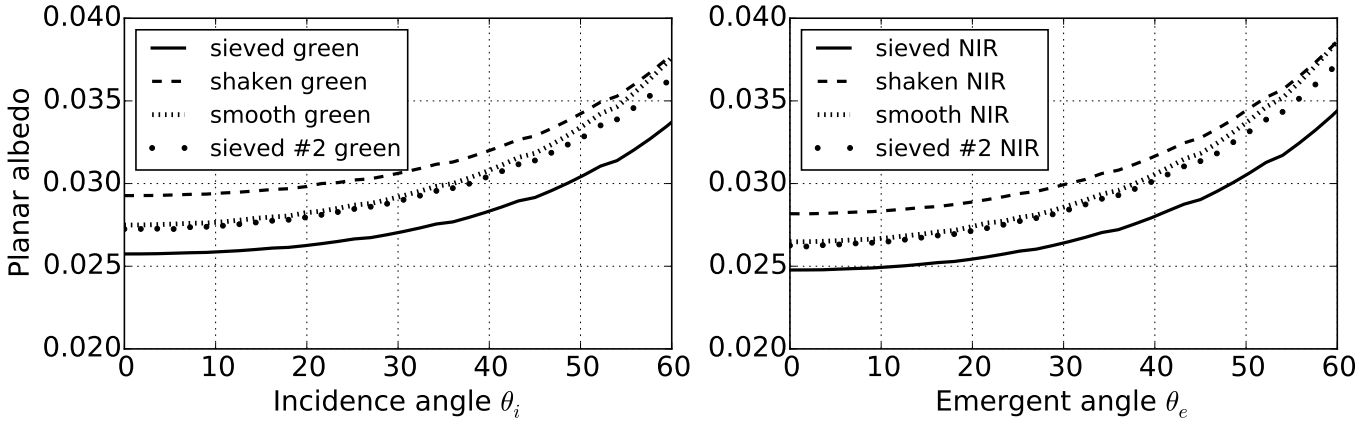


Figure 11: The plane albedo as a function of incidence angle for the eight different models. The four different surface treatments correspond to different shadowing corrections, and the two different spectral bands to different phase functions.

such a large increase cannot be indicative of the true packing density. This is further shown by the fact that after smoothing, the sample is fit with lower packing density again. Previous laboratory results and theoretical considerations say that an increase in packing density should cause an increase in the albedo of the surface [23, 9]. This is also observed in our measurements. Since our modelling considers only one type of size distribution and the volume-element albedo is assumed not to depend on the packing, an increase in brightness can only be modelled as an increase in packing density. The shaking may cause effects such as changes in the surface size distribution, which cannot therefore be separated from the modeled packing density.

All the measurements show a darkening trend at high angles of emergence in the backward direction, compared to the models. This is partly due to the experimental setup. In the PM scattering model, this kind of behaviour is produced by high surface roughness. Quantifying the surface roughness in the real samples is very difficult, however, and drawing strong conclusions on the samples' roughness properties is not possible.

All of the best fits for the first three measurements result in rather high values for the roughness amplitude $\sigma$, which indicates deep roughness features compared to the particle scale. The direct interpretation of the large $\sigma$ values into real world units is larger than the apparent roughness of the sample. This suggests that a more detailed study of the combined effect of the roughness and the size distribution in the PM model is needed. The other weaknesses of the currently available version of the PM scattering model are the finite angular resolution and the numerical noise due to the Monte Carlo method used in its precomputations. All these are technical limitations which can be improved with some additional computational effort, which is outside the scope of the present measurement-oriented study.

Another unexpected observation is that the second sample which was sieved onto the measurement plate has a BRF much more similar to first sample smoothed, rather than sieved. Conclusions on this are also limited by the difficulties in sample characterization. The sieving was performed by the same person and in the same way both times. It appears that the distribution of particles resulting from the sieving can vary enough to cause significant changes in the BRF.

Though the volcanic sand has a rather flat spectrum in the visible-NIR range, the NIR end shows clearly stronger forward scattering and weaker backward scattering than the green end. The geometric albedo is correspondingly higher in the green band. The higher value $p = 0.043$ is still quite low, but these values are also likely underestimated because of the lack of data near exact opposition.

All in all, we find that good measurements of dark regolith-like materials can be obtained with the

FIGIFIGO instrument, and that the semi-numerical PM scattering model can match the features of the measured data well with a reasonable phase function. Better measurements are needed to improve the physical interpretation of the PM scattering model parameters, but controlling the parameters even for a laboratory sample is challenging. A more detailed laboratory measurement campaign in the future could produce a data set of parametrizations of different regolith analogues for comparisons with remote sensing data of Solar System objects.

## Acknowledgements

The research was partly funded by the Academy of Finland projects 257966 and 260027, and the ERC Advanced Grant No 320773 entitled Scattering and Absorption of Electromagnetic Waves in Particulate Media (SAEMPL). We thank Teemu Hakala for his expert assistance with the FIGIFIGO instrument.

We thank P. Dagsson Waldhauserová, O. Arnalds, A. Virkkula, O. Meinander, and J. Svensson for their help with obtaining the samples and relevant discussions. MG acknowledges support from the COST Action ES1404 "A European network for a harmonised monitoring of snow for the benefit of climate change scenarios, hydrology and numerical weather prediction" which enabled collection of the volcanic sand sample in Iceland for intensive laboratory research. The research at the UrFU are supported by the Government of the Russian Federation (Act 211, agreement 02.A03.21.0006).

We thank the reviewers, Bruce Hapke, Paul Helfenstein and Yuriy Shkuratov, for their comments which helped us improve this paper.

## References

## References

[1] Arnalds, O., 2010. Dust sources and deposition of aeolian materials in Iceland 23 (1), 3–21.

[2] Arnalds, O., Dagsson-Waldhauserova, P., Olafsson, H., 2016. The Icelandic volcanic aeolian environment: Processes and impacts — A review. Aeolian Research 20, 176–195.

[3] Bondarenko, S., Ovcharenko, A., Shkuratov, Y., Videen, G., Eversole, J., Hart, M., jun 2006. Light backscatter by surfaces composed of small spherical particles. Applied Optics 45 (16), 3871.

[4] Bus, S. J., Vilas, F., Barucci, M. A., 2002. Visible-Wavelength Spectroscopy of Asteroids. Asteroids III.

[5] Cord, A. M., Pinet, P. C., Daydou, Y., Chevrel, S. D., oct 2003. Planetary regolith surface analogs: optimized determination of Hapke parameters using multi-angular spectro-imaging laboratory data. Icarus 165 (2), 414–427.

[6] Domingue, D. L., Denevi, B. W., Murchie, S. L., Hash, C. D., 2016. Application of multiple photometric models to disk-resolved measurements of Mercury's surface: Insights into Mercury's regolith characteristics. Icarus 268, 172–203.

[7] Fairbairn, M. P., 2005. Planetary Photometry: the Lommel-Seeliger law. Journal of the Royal Astronomical Society of Canada 99.

[8] Hakala, T., 2009. Improvements, Calibration, and Accuracy of the Finnish Geodetic Institute Field Goniospectrometer. M.sc. thesis, Helsinki University of Technology.

[9] Hapke, B., 2008. Bidirectional reflectance spectroscopy. 6. Effects of porosity. Icarus 195 (2), 918–926.

[10] Hapke, B., 2012. Theory of reflectance and emittance spectroscopy, 2nd Edition. Cambridge University Press.

[11] Johnson, J. R., Shepard, M. K., Grundy, W. M., Paige, D. A., Foote, E. J., mar 2013. Spectrogoniometry and modeling of martian and lunar analog samples and Apollo soils. Icarus 223 (1), 383–406.

[12] Kaasalainen, M., Mottola, S., Fulchignoni, M., 2002. Asteroid Models from Disk-integrated Data. In: Bottke, W. F. J., Cellino, A., Paolicchi, P., Binzel, R. (Eds.), Asteroids III. The University of Arizona Press, Tucson, AZ, pp. 139–150.

[13] Li, J.-Y., Helfenstein, P., Buratti, B. J., Takir, D., Clark, B. E., 2015. Asteroid Photometry. In: Michel, P., DeMeo, F. E., Bottke, W. F. (Eds.), Asteroids IV. University of Arizona Press, Tucson, AZ, pp. 129–150.

[14] Lumme, K., Bowell, E., nov 1981. Radiative transfer in the surfaces of atmosphereless bodies. I - Theory. The Astronomical Journal 86, 1694.

[15] McKay, D., Heiken, G., Basu, A., Blanford, G., Simon, S., Reedy, R., French, B. M., Papike, J., 1991. The Lunar Regolith. In: Lunar Sourcebook. Cambridge University Press, Cambridge, pp. 285–356.

[16] McKay, D. S., Carter, J. L., Boles, W. W., Allen, C. C., Allton, J. H., 1993. JSC-1: A new lunar regolith simulant. In Lunar and Planetary Inst. Twenty-Fourth Lunar and Planetary Science Conference, 963–964.

[17] Meinander, O., Kontu, A., Virkkula, A., Arola, A., Backman, L., Dagsson-Waldhauserová, P., Järvinen, O., Manninen, T., Svensson, J., de Leeuw, G., Leppäranta, M., may 2014. Brief communication: Light-absorbing impurities can reduce the density of melting snow. The Cryosphere 8 (3), 991–995.

[18] Näränen, J., Kaasalainen, S., Peltoniemi, J., Heikkilä, S., Granvik, M., Saarinen, V., nov 2004. Laboratory photometry of planetary regolith analogs. Astronomy and Astrophysics 426 (3), 1103–1109.

[19] Peltoniemi, J., Hakala, T., Suomalainen, J., Puttonen, E.,

nov 2009. Polarised bidirectional reflectance factor measurements from soil, stones, and snow. Journal of Quantitative Spectroscopy and Radiative Transfer 110 (17), 1940–1953.

[20] Peltoniemi, J. I., Gritsevich, M., Hakala, T., Dagsson-Waldhauserová, P., Arnalds, Ó., Anttila, K., Hannula, H.-R., Kivekäs, N., Lihavainen, H., Meinander, O., Svensson, J., Virkkula, A., de Leeuw, G., dec 2015. Soot on Snow experiment: bidirectional reflectance factor measurements of contaminated snow. The Cryosphere 9 (6), 2323–2337.

[21] Peltoniemi, J. I., Gritsevich, M., Puttonen, E., 2015. Reflectance and polarization characteristics of various vegetation types. In: Kokhanovsky, A. (Ed.), Light Scattering Reviews 9. Springer Berlin Heidelberg, Berlin, Heidelberg, pp. 257–294.

[22] Peltoniemi, J. I., Hakala, T., Suomalainen, J., Honkavaara, E., Markelin, L., Gritsevich, M., Eskelinen, J., Jaanson, P., Ikonen, E., oct 2014. Technical notes: A detailed study for the provision of measurement uncertainty and traceability for goniospectrometers. Journal of Quantitative Spectroscopy and Radiative Transfer 146, 376–390.

[23] Shepard, M. K., Helfenstein, P., mar 2007. A test of the Hapke photometric model. Journal of Geophysical Research 112 (E3), E03001.

[24] Shkuratov, Y., feb 1999. A Model of Spectral Albedo of Particulate Surfaces: Implications for Optical Properties of the Moon. Icarus 137 (2), 235–246.

[25] Shkuratov, Y., oct 2002. The Opposition Effect and Negative Polarization of Structural Analogs for Planetary Regoliths. Icarus 159 (2), 396–416.

[26] Svensson, J., Virkkula, A., Meinander, O., Kivekäs, N., Hannula, H.-R., Järvinen, O., Peltoniemi, J. I., Gritsevich, M., Heikkilä, A., Kontu, A., Neitola, K., Brus, D., Dagsson-Waldhauserova, P., Anttila, K., Vehkamäki, M., Hienola, A., De Leeuw, G., Lihavainen, H., 2016. Soot-doped natural snow and its albedo — results from field experiments. Boreal Env. Res 21, 481–503.

[27] Wilkman, O., Muinonen, K., Peltoniemi, J., jun 2015. Photometry of dark atmosphereless planetary bodies: an efficient numerical model. Planetary and Space Science 118, 250–255.

[28] Wilkman, O., Muinonen, K., Videen, G., Josset, J.-L., Souchon, A., oct 2014. Lunar photometric modelling with SMART-1/AMIE imaging data. Journal of Quantitative Spectroscopy and Radiative Transfer 146, 529–539.

[29] Zubko, N., Gritsevich, M., Zubko, E., Hakala, T., Peltoniemi, J. I., dec 2015. Optical measurements of chemically heterogeneous particulate surfaces. Journal of Quantitative Spectroscopy and Radiative Transfer (178), 422–431.